Numerical analysis of an optimal metal wool-phase change material for thermal energy storage with exceptionally high power density

Applied Thermal Engineering 273 (2025) 126429

Contents lists available at ScienceDirect

Applied Thermal Engineering

journal homepage: www.elsevier.com/locate/ate

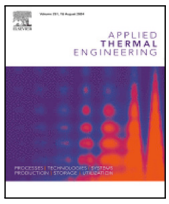

Research Paper

Numerical analysis of an optimal metal wool-phase change material for thermal energy storage with exceptionally high power density

Alessandro Ribezzo [a], Matteo Morciano [a], Gabriel Zsembinszki [b], Saranprabhu Mani Kala [b], Emiliano Borri [b], Luca Bergamasco [a], Matteo Fasano [a], Eliodoro Chiavazzo [a,*], Cristina Prieto [c], Luisa F. Cabeza [b,*]

[a] Department of Energy, Politecnico di Torino, Corso Duca degli Abruzzi 24, 10129, Torino, Italy
[b] GREiA Research Group, University of Lleida, Pere de Cabrera s/n, 25001, Lleida, Spain
[c] University of Seville, Department of Energy Engineering, Camino de los Descubrimientos s/n, 41092, Seville, Spain

ARTICLE INFO

Keywords:
Phase change materials
Thermal energy storage
Heat transfer enhancement
Numerical simulations
Metal wool

ABSTRACT

The adoption of thermal energy storage (TES) systems based on phase change material (PCM) remains limited by their low thermal conductivity, which restricts power density. Existing heat transfer enhancement techniques are often costly or come with significant drawbacks, leaving a gap for an effective and affordable solution. This study highlights metal wool as a promising alternative, offering low cost, ease of application, and retrofitting potential. While previous experiments demonstrated substantial improvements in power density using copper wool, a comprehensive numerical model to further optimize this technique is presented here. The model, incorporating CFD simulations and uncertainty analysis, was validated for bulk PCM and two copper wool-PCM composites before being extended to a wool material analysis. First, possible alternatives to copper as wool material were tested, highlighting aluminum as a viable candidate. Then, the proposed composite was found to match the discharging performance of a PCM with an effective thermal conductivity of 2.5 W/mK, a value rarely achieved by conventional enhancement techniques. Additionally, a techno-economic comparison revealed that copper wool delivered a 14.7-fold increase in thermal conductivity relative to liquid PCM at €6 per kg of PCM additivated—a performance unmet by metal foams and nanocomposites. These findings confirm metal wool as a viable cost-effective and high-performance solution for improving TES systems, partially bridging the gap between efficiency and affordability.

1. Introduction

The major shift in global energy paradigms resulting from the transition to renewable energy sources [1] necessitates technologies that offer flexibility between energy supply and demand, as the latter is generally variable (or inflexible, in the case of nuclear energy), and it does not match the demand side. In this context, thermal energy storage (TES) technologies are part of a wider portfolio that is available for obtaining such flexibility, thus overcoming the operational challenges associated with the high integration of intermittent energy sources.

Among TES, latent heat storage (LHS) technologies are a promising solution. Compared to sensible heat storage, LHS systems offer the main advantage of storing a relatively large amount of thermal energy within a narrow temperature range (across their phase transition temperature). Thus, LHS offers significant advantages in applications requiring temperature stabilization or high energy-density storage solutions [2]. This technology relies on phase change materials (PCMs), which store thermal energy primarily in the form of transition enthalpy between two phases. Contrarily to sensible heat storage materials, which absorb or release thermal energy in proportion to their temperature changes, mass, and specific heat capacity, the temperature of PCMs remains constant during the phase change process, enabling (ideally) isothermal heat transfer within the material.

Among the key properties (e.g. no chemical degradation, compatibility with surrounding materials, non-toxicity, non-flammability, nonexplosivity, modest density variation during the phase transition, low vapor pressure at the operating temperature, and no physical separation [3]) that are required for enabling the adoption of PCMs extensive use in real-world applications, the low thermal conductivity is widely known as one of the major bottlenecks, especially in those applications that require a high power density [1]. Such low thermal conductivity generally limits the rate at which thermal energy is

* Corresponding authors.
E-mail addresses: eliodoro.chiavazzo@polito.it (E. Chiavazzo), luisaf.cabeza@udl.cat (L.F. Cabeza).

https://doi.org/10.1016/j.applthermaleng.2025.126429
Received 4 February 2025; Received in revised form 27 March 2025; Accepted 2 April 2025
Available online 11 April 2025

Nomenclature

ΔT	Half of the mushy zone (K)
Δx_{ord}	Porous size (m)
λ_{HTF}	HTF thermal conductivity (W/m/K)
λ_l	Liquid PCM thermal conductivity (W/m/K)
λ_s	Solid PCM thermal conductivity (W/m/K)
μ	PCM dynamic viscosity (Pa s)
μ_{HTF}	HTF dynamic viscosity at fluid temperature (Pa s)
$\mu_{HTF,wall}$	HTF dynamic viscosity at wall temperature (Pa s)
ρ_l	Liquid PCM density (kg/m^3)
ρ_s	Solid PCM density (kg/m^3)
ϵ	Porosity term small constant (–)
A	Porosity term (kg/m^3/s)
A_2	Porosity term for the viscosity (–)
C	Porosity term constant (kg/m^3/s)
D	Sensitivity analysis target function (K^2)
D_{dis}	Corrective term to consider the disordered configuration (–)
d	Tube diameter (m)
d_{sensor}	Sensor distance from the HTF tube (m)
f	Liquid phase fraction (–)
$\mathbf{F}_g$	Additional momentum term for the buoyancy effect (N/m^3)
$\mathbf{F}_u$	Additional momentum term for velocity reduction (N/m^3)
F	Random function (–)
$\mathbf{g}$	Gravitational acceleration (m/s^2)
h	Heat transfer coefficient (W/m^2/K)
L	PCM latent heat (J/kg)
L_{sensor}	Sensor length (m)
p	Pressure (Pa)
P	Thermal conductivity penalization term (–)
Pr	Prandtl number (–)
Re	Reynolds number (–)
T_{exp_i}	Experimental temperature at time i (K)
$T_{initial}$	PCM initial temperature (K)
T_{num_i}	Numerical temperature at time i (K)
T_{pc}	PCM phase transition temperature (K)
$\mathbf{v}$	PCM velocity (m/s)
x_{disord}	Fiber edge position in the disordered configuration (m)
x_{ord}	Fiber edge position in the ordered configuration (m)

transferred in the material, thus leading to prolonged charging and discharging times in TES systems, an issue also known as the rate problem [4]. This issue becomes especially noticeable during the solidification of PCMs when the interface between the liquid and solid phases forms at the heat transfer surface and gradually moves away, resulting in a solid PCM layer of increasing thickness. This layer enhances thermal resistance by acting as an insulator due to the inherently low thermal conductivity of PCMs, leading to a self-insulating effect [5]. Therefore, the discharging processes of PCMs are generally much longer than the charging ones. In cases of partial melting/solidification, latent TES may even be disadvantageous as compared to sensible TES in practical applications [6,7].

Several strategies have been studied in the literature to mitigate this limitation by enhancing the heat transfer in PCM-based applications. These techniques can be classified as static or flexible. In the former case, heat transfer is improved through fixed, stationary layouts, whereas in the latter, the highly conductive nanofillers, incorporated into the low-conductivity PCM matrix, move along with it. The static standard technique is obtained by strategically placing fins within the PCM container [8,9]. This technique may significantly both increase the heat transfer surface area and create different heat transfer surfaces at which the phase transitions initiate, thus reducing the local thickness of the bulk PCM that acts as an insulator [10,11]. However, this reduction in space available leads also to a diminished natural convection that generally speeds up the melting process. These two contrasting phenomena resulting from the reduction in available space for PCMs govern the overall impact of the fins on the charging and discharging processes, thus requiring specific analysis for the different case studies [12]. A general remark highlighted by the literature studies was the importance of the length and number of fins rather than their thickness and orientation [13]. Beyond the potential benefit of reducing charging and discharging times in PCM-based TES tanks, this technique also comes with several drawbacks. First, a general reduction of the PCM amount is needed to obtain the space for the fins, thus reducing the energy density and nominal energy capacity of the storage system. Moreover, the fins addition generally causes a relevant increase in the mass of the storage system [14], and leads to more complex designs and manufacturing. Finally, this technique cannot be adopted in already-built TES tank solutions, as it has to be performed at the design stages.

Regarding the main flexible technique, i.e. the use of PCM nanocomposites, the concept is to improve the effective thermal conductivity of the PCM at the material scale and create a more efficient path for heat transfer within the material [15]. In this context, numerous studies have investigated experimentally, computationally, and analytically the effects of various nanofillers — including metallic and carbon-based [16,17] — within PCM matrices [15,18]. These studies explored the resulting variations in melting and solidification behavior under different conditions, such as TES tank size and shape [19,20], as well as in diverse applications, including domestic heating [21], thermal management [22], and solar thermal storage [23]. Nonetheless, this technique, which theoretically could achieve sufficiently high thermal conductivities with a modest amount of nanofiller, has not yet reached the expected outcomes due to various issues. First, the heat transfer within the composite material is severely hindered by the thermal resistances generated at the interfaces between the nanoparticles and the bulk PCM and between different nanoparticles. Such thermal resistances are caused by phenomena at different scales occurring at the interfaces of different materials, such as air inclusions due to non-perfect adhesion (which results in smaller effective contact areas between the two components) [24], and phonon scattering caused by spectral mismatches [25]. Moreover, traditional additivation techniques used to produce these composite materials often result in unstable composites. When the PCM is in its liquid phase, the large density differences between the matrices and additives cause phase segregation of the nanofillers. Finally, most of the nanofillers, such as the carbon-based ones (graphene nanoplatelets and carbon nanotubes) are orders of magnitude more expensive than commercial PCMs [26].

The difficulty in managing such nanocomposites and the fins-related drawbacks called forth innovative heat transfer enhancement techniques. In this context, a promising technique regards the integration of metal foams into the PCM matrices. Metal foams are generally characterized by a low-weight highly porous structure (porosity values usually larger than 95%) [27] which can be tailored to specific porosities and pore densities to optimize heat transfer rates [28]. Here, the heat transfer enhancement is obtained by increasing the heat transfer surface area and generating several phase transition initiation surfaces with the consequent decrease in the local thickness of bulk PCM. Therefore, more efficient heat conduction and consequent uniform temperature distribution are present within the PCM [29]. Compared to nanocomposites, such a technique does not present segregation issues and was also reported to perform more effectively [30]. With respect to fins, on the other hand, metal foams, being porous materials, require a lower

amount of space, thus leading to greater energy densities as a larger PCM mass can be inserted. However, the porous structure leads to a dramatically low space for the PCM liquid phase movement, thus almost suppressing the natural convection during the melting process. The use of these structures also presents other challenges, primarily related to optimizing porosity and pore density, which have been reported to produce conflicting effects on thermal performance, particularly in terms of charging and discharging times of the thermal battery [30]. More importantly, their manufacturing processes are complex and their costs are remarkably higher than the ones possessed by most of the PCMs.

In the context here presented, metal wools may overcome critical drawbacks possessed by the previously described heat transfer enhancement techniques, as they represent a promising relatively low-cost, easy-to-implement, and effective solution that has not been extensively studied in the literature. Metal wools are highly porous (porosity larger than 90%), stable, and flexible structures made of metallic fibers entangled among them. By possessing a structure similar to that of metal foams, metal wools possess similar characteristics: they provide a three-dimensional highly conductive pathway within the PCM, increase the heat transfer surface area, generate several phase transition initiation surfaces, and reduce the nominal energy capacity of the TES system of a minor extent. Besides their similarities, foams and wools differ as (i) even if wools are stable, they can be easily shaped in different forms, being flexible, thus also possibly representing an ideal candidate solution for retrofitting existing thermal batteries, and (ii) wools manufacturing is way easier (and cheaper) than that of foams. Metal wools, in fact, have been produced for decades and are available in the market for construction, shielding, damping, and other applications [31]. For these reasons, metal wool costs are much lower than that of metal foams, thus reducing the relative economic impact of the additive technique [31]. Different wool materials are available in the market, such as aluminum, stainless steel, copper, brass, and also disposable materials have been proposed in the scientific literature [32]. With these solutions, the heat transfer enhancement that can be achieved is a function of the geometry of the fibers and their alignments, as well as the orientation of the overall structure within the PCM-based TES tank. In fact, metal wools can be shaped into fin-like shapes thanks to their flexibility, with the modest decrease of space available for the PCM related to the presence of a highly porous structure. More importantly, they can also be used in already-built TES tanks. In summary, metal wools (i) do not present the managing challenges required by the nanofiller additivation, (ii) require a lower volume compared to the fins, and (iii) are much simpler (and cheaper) than the metallic foam from the manufacturing point of view. The mentioned advantages make metallic wools an attractive option for those large-scale applications that need a flexible, easy-to-implement, and low cost solution, especially in already existing storage systems (retrofit). This technology could be particularly well-suited for retrofitting PCM-based TES tanks that utilize a heat exchanger configuration, which is the most common layout [33]. This design is especially advantageous for applications requiring a combination of high energy and power densities. As a result, this technology could be integrated into applications that demand high power and short charging/discharging cycles, such as the power [34], heating and cooling [35], and industrial [36] sectors.

Despite the above interesting items, to our knowledge, metal wools have been poorly investigated in the current literature. At the material scale, the effective thermal conductivity of an inert resin-stainless steel wool composite was studied by Prieto et al. [37]. A casting method and an infiltration technique were tested, and only the latter was reported as a successful production technique. The composite effective thermal conductivity was experimentally obtained by means of a transient plane source hot-disk technique. The introduction of 10% in volume of metallic wool resulted in effective thermal conductivities of 4 W/m K and 0.77 W/m K in the fibers' radial and axial directions, respectively. At lab scales, few TES tanks have been analyzed. The impact of a steel wool was assessed in a shell and tube configuration TES tank by studying two different wool configurations: a uniform wool dispersion and a fins-like shape [38]. Here, modest reductions in charging times and negligible impacts on discharging times were reported. In [39], a simplified configuration consisting of a sole tube of a shell and tube TES tank was adopted for studying the melting and solidification behaviors of a salt PCM additivated by a stainless steel wool for high-temperature applications. An effective thermal conductivity of 2 W/m K of the wool composite was obtained by means of comparison between numerical simulations and experimental measurements with 10% wool volume content, a 300% increase with respect to the bulk PCM thermal conductivity. Finally, Khliyeva et al. [40] adopted a simplified geometry for testing two different wool materials (copper and aluminum) to assess their impact on the melting and solidification behavior of a paraffin PCM. Promising results were reported, with copper performing better than aluminum. The discrepancies reported by the described literature results may be due to the different production procedures of the wool available in the market, which severely affect its structure, geometrical, and thermophysical properties.

A comprehensive study of the charging and discharging process of a metal wool-PCM composite in a TES tank is needed, as the previously described studies gave a partial framework, by focusing on simplified TES tank geometries [39,40], material properties characterization [37], or preliminary wools pattern [38]. To this aim, we carried out an experimental campaign by testing different copper wool patterns and fiber dimensions, in order to assess their impact on the charging and discharging behaviors of a PCM-based TES tank prototype. The results of this experimental analysis, which are reported in Ribezzo et al. [41,42] and Kala et al. [43], stressed how metal wools may be an effective heat transfer enhancement technique, by showing outstanding improvements, especially during the discharging process. These experimental studies, which have studied different wool configurations within the TES tank, have also suggested the possibility of defining optimized solutions, both in terms of wool configuration and material.

In this context, this study aims to carry out a numerical analysis of metal wool as a viable heat transfer enhancement technique in PCM-based TES systems. CFD simulations have been first validated by means of a comparison with experimental tests and then utilized to explore possible improvements in wool materials and configurations. The CFD simulations have been coupled with an optimization software to explore the design space of the input parameters (thermophysical and geometrical properties), thus assessing the impact of such inputs on the numerical outcome. Configurations containing bulk PCM and two copper wool-PCM composites have been considered in the numerical analysis. The composites have been obtained by adding thick and fine fiber wool sheets perpendicularly to the heat transfer fluid tubes of the TES tank, with corresponding packing factors of 0.24 and 0.22 g/cm^3. For the comprehensive description of these configurations and their corresponding experimental results refer to cases 1 and 3 of [43], where three charging/discharging cycles were conducted for both configurations with different packing factors, and the average values were taken from these tests, showing only minor variations with small error bars. Useful insights were obtained from this numerical analysis about the thermal performance (namely the discharging time) of such PCM-wool composites in terms of possible cheaper alternatives to copper as wool material, and preliminary comparison from an economic perspective with other heat transfer enhancement techniques, such as nanocomposites and metal wools. To the best of the authors' knowledge, no studies have conducted such a comprehensive numerical analysis of copper wool as a heat transfer enhancement technique in PCMs for TES within the scientific literature. Furthermore, this study introduces the proposed heat transfer enhancement approach in the context of a shell-and-tube TES tank configuration. The proposed system may be integrated into TES applications requiring relatively high power and energy densities, such as in the automotive sector [8], as well as for localized or small-scale cooling and heating [44] and waste heat recovery [45].

2. Theoretical framework

2.1. Enthalpy-porosity approach

CFD simulations of the thermal behavior of the PCM have been performed by means of COMSOL Multiphysics. Simplifying assumptions were used to decrease the computational effort. First, only a subsystem of the entire TES tank was considered, which consists of a vertical pair of tubes. Moreover, a 2D section was considered, thus assuming that the variation of the PCM behavior along the length of the HTF tubes was negligible. These two simplifying assumptions were adopted due to the geometrical symmetry of the TES tank and the high velocity of the HTF. Under these conditions, it was reasonable to consider each couple of tubes' behavior as almost symmetrical with respect to the others. A boundary condition at the tube-PCM boundaries was introduced to simulate the heat transfer between the HTF and copper tubes. Specifically, convective heat flux caused by internal forced convection in an isothermal tube was considered. This boundary condition was chosen in order to obtain a balance between the physical accuracy and computational efficiency of the numerical model, thus avoiding the complexity of solving full fluid dynamics inside the tubes, as the primary focus was the PCM behavior. The inlet temperature and mass flow rate of the HTF were taken from the experimental values detected by the temperature sensor and the flow meter. The heat transfer coefficient used to define this boundary condition was obtained as [46]:

$$h = \begin{cases} \frac{\lambda_{HTF}}{d} 3.66, & \text{if } Re_d \le 2500 \\ \frac{\lambda_{HTF}}{d} 0.027 Re_d^{4/5} Pr^{1/3} \left(\frac{\mu_{HTF}}{\mu_{HTF,wall}}\right)^{0.14}, & \text{if } Re_d > 2500 \end{cases}$$

where d is the internal diameter of the HTF tube, Re the Reynolds number, Pr the Prandtl number, λ_{HTF} the thermal conductivity of the HTF, and μ_{HTF} and $\mu_{HTF,\ wall}$ the dynamic viscosity of the HTF at the fluid and wall temperature, respectively. Symmetrical and insulating heat transfer boundary conditions were imposed at the horizontal and vertical boundaries, respectively. Regarding the fluid flow physics, wall and symmetry boundary conditions were adopted at the horizontal and vertical boundaries, respectively, and a pressure value was imposed at the left-upper angle. As an initial condition, at the time $t = 0$, the PCM was supposed at a homogeneous temperature $T_{initial}$. A schematic overview of the whole 3D TES tank and the 2D subsystem considered in the numerical simulations are shown in Fig. 1, along with the boundary conditions applied.

The thermal behavior of the PCM was simulated by the enthalpy-porosity method [47]. This approach is based on the coupling between the enthalpy, continuity, and momentum equations to model the thermal behavior of the solid and liquid phases, the phase transition, and the movement of the PCM liquid phase due to natural convection. According to it, the following equations are considered:

$$\rho_l \nabla \cdot \mathbf{v} = 0, \tag{1}$$

$$\rho_l \frac{\partial \mathbf{v}}{\partial t} + \rho_l(\mathbf{v}\cdot\nabla)\mathbf{v} = \nabla \cdot [-p\mathbf{I} + \mathbf{K}] + \mathbf{F}_g + \mathbf{F}_u, \tag{2}$$

$$\rho_l c_p(T)\left(\frac{\partial T}{\partial t} + \mathbf{v}\cdot\nabla T\right) = \nabla\cdot(\lambda(T)\nabla T) + S_h, \tag{3}$$

where

$$\mathbf{K} = \mu(T)(\nabla\mathbf{v} + (\nabla\mathbf{v})^T), \tag{4}$$

$$\mathbf{F}_u = -A(f)\cdot\mathbf{v}, \tag{5}$$

$$\mathbf{F}_g = [\rho_l + \left(\frac{\rho_l - \rho_s}{2\Delta T}\right) T - (T_{pc} + \Delta T)]\mathbf{g}, \tag{6}$$

$$S_h = -\rho_l L \frac{df}{dt}. \tag{7}$$

$\mathbf{F}_g$ is an additional momentum term for considering the buoyancy effect, where $\mathbf{g}$ is the gravitational acceleration and ΔT half of the mushy zone. $\mathbf{F}_u$ is an additional momentum term to include the gradual reduction of the velocity from the liquid value to zero (fully solid PCM) in the mushy zone. According to this method, in fact, the portion of liquid material that is within the mushy zone is modeled as a fluid flow in a porous medium, in which the porosity term $A(f)$ of Eq. (5) is defined according to the Carman–Kozeny equation for flow in porous media [48]:

$$A(f) = \frac{C(1-f)^2}{(f^3 + \epsilon)}, \tag{8}$$

where ϵ is a small constant (1e−3) included for computational purposes, while C is a constant for modeling the structure of the melting front, whose value is still undefined in the scientific literature, ranging from 10^4 to 10^8 [47]. S_h of Eq. (7) is the additional energy term introduced to include the PCM latent heat contribution, where $f(T)$ is the liquid fraction, whose value is 0 in the fully solid region and 1 in the fully liquid region, while it is generally assumed to vary linearly in the mushy zone, even if detailed mushy zone variation curves are emerging from DSC analysis [49]. The thermal conductivity λ and specific heat capacity c_p were considered to vary linearly between their solid (subscript s) and liquid (subscript l) values as a function of the temperature:

$$\lambda = \lambda_l + \left(\frac{\lambda_l - \lambda_s}{2\Delta T}\right)(T - (T_{pc} + \Delta T)), \tag{9}$$

$$c_p = c_{p,l} + \left(\frac{c_{p,l} - c_{p,s}}{2\Delta T}\right)(T - (T_{pc} + \Delta T)), \tag{10}$$

while the dynamic viscosity μ varied between its liquid value μ_l and a very large value in the solid phase to avoid any movement:

$$\mu = \mu_l(1 + A_2(f)). \tag{11}$$

The solid and liquid values in Eqs. (9), (10), and (11) were assumed constant within their respective phases over the considered temperature range, as experimental testing indicated modest variations of these properties for the PCM material under study [50] in these conditions.

2.2. Exploration algorithm

A relevant issue in getting reliable results from numerical simulations is due to the PCMs thermophysical (and TES tank geometrical) properties provided as input in the numerical model. An important source of errors, in fact, may derive from the uncertainty of these parameters, which may attributed to [51]: the difficulty in finding consistent thermophysical properties measurements due to different techniques [3,52], and the scaling up to mesoscale applications of these experimental values obtained at microscopic scales [3].

In this context, an analysis that considers the uncertainty of these input values may lead to more accurate results and the identification of the most sensitive input parameters. For these reasons, the CFD simulations have been coupled with an optimization software, ModeFrontier [53], to assess the impact of the uncertainty of the input parameters on the output of the numerical simulations. This analysis was obtained by emulating the working mechanism of the temperature sensor in the numerical model. Since Resistance Temperature Detectors (RTDs) were used as sensors in the experiments, the numerical model incorporated a vertical line of length L_{sensor} at a distance d_{sensor} from the tube, along which the temperature average was computed throughout the charging/discharging process. This numerical approach was employed to replicate the working mechanism of RTD sensors in the simulations, as these sensors measure the temperature of the medium they are embedded in by averaging the values detected along their pin length. Being the solidification of the PCM the major physical bottleneck in most of the applications, as it reduces the power density and increases remarkably the charging/discharging cycle duration, this

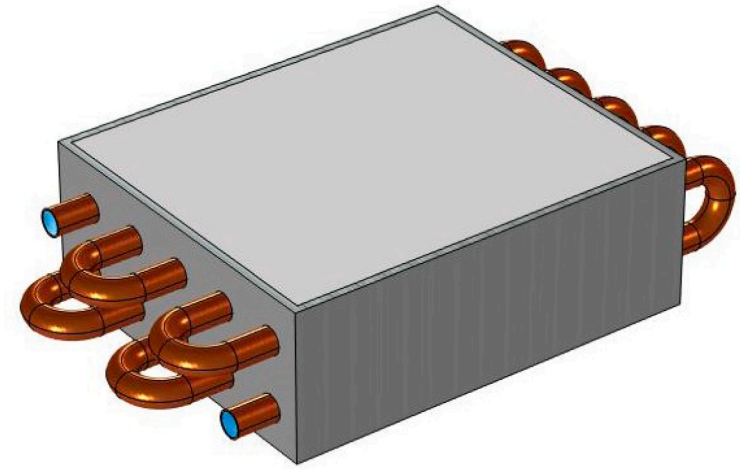

(a)

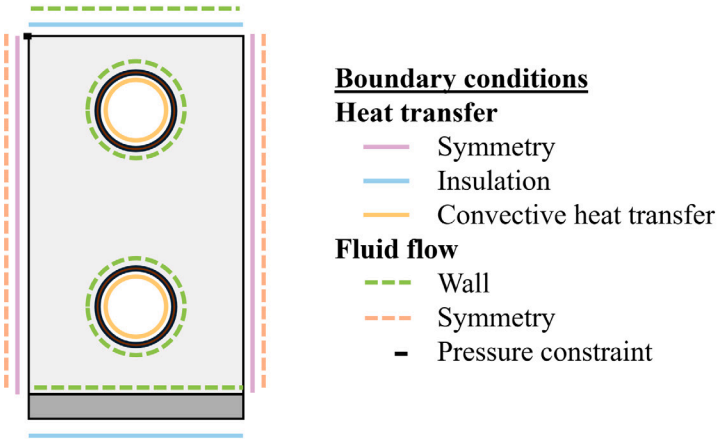

(b)

Fig. 1. Schematic of the whole 3D TES tank (a), and the two-dimensional subsystem considered in the CFD simulations, along with the applied boundary conditions applied (b).

process was chosen as the main focus of the numerical simulations. It is important to stress that, in this study in which a storage application was not defined, the convention adopted was charging-melting, discharging-solidification. The PCM-related parameters, i.e. latent heat L, melting temperature T_{pc}, phase transition window ΔT, dynamic viscosity μ_l, thermal conductivity and specific heat capacity in both liquid and solid phases λ_l, λ_s, $c_{p,s}$, $c_{p,l}$, were considered to vary of $\pm 5\%$ from the nominal values experimentally obtained at the material scale for the reasons previously described, i.e. the difficulty in finding consistent thermophysical properties values and the scaling up issue. Additionally, L_{sensor} and d_{sensor} were allowed to vary between their possible extreme positions detected during the experiments. Finally, the constant C of the enthalpy-porosity method shown in Eq. (8) was considered in the range 10^4–10^8. Table 1 is an overview of the considered ranges (and information sources) of the various input parameters in the case of bulk PCM.

This sensitivity analysis was obtained by means of SOBOL, a deterministic design of experiment algorithm that varies the input parameters to obtain a uniform sampling of the design space and reduce the clustering effect [53]. As described before, the output of the numerical simulations was chosen as the temperature average along the line introduced to mimic the temperature sensor. In this context, the target function of the sensitivity analysis was the discrepancy between the temperature-discharging time curves obtained from experimental measurements and numerical simulations. This value was computed as

Table 1
Overview of the ranges of the various properties considered in the exploratory numerical analysis.

Property	Range	Source
T_{pc} [°C]	26.6 ± 5%	DSC analysis [41]
L [J/g]	202.5 ± 5%	DSC analysis [41]
ΔT [K]	1.47 ± 5%	DSC analysis [41]
d_{sensor} [mm]	0.9–1.8	Exp. measurements
L_{sensor} [mm]	4-5.8	Exp. measurements
λ_l [W/m K]	0.17 ± 5%	From literature [50,54]
λ_s [W/m K]	0.29 ± 5%	From literature [50,54]
μ_l [mPa s]	3 ± 5%	From literature [50,54]
$c_{p,s}$ [J/kg K]	1750 ± 5%	From literature [50,54]
$c_{p,l}$ [J/kg K]	2200 ± 5%	From literature [50,54]
C [–]	10^4–10^8	From literature [47,55]

the sum of the square of the difference between the numerical and experimental values detected at each measurement instant:

$$D = \sum_{i=0}^{N} (T_{exp_i} - T_{num_i})^2, \tag{12}$$

where N is the total number of time steps of the discharging process, and T_{exp_i} and T_{num_i} are the experimental and numerical temperatures at time step i, respectively. T_{exp_i} was obtained by averaging the outputs of the temperature sensors contained in the PCM side of the TES tank, as described in [42,43].

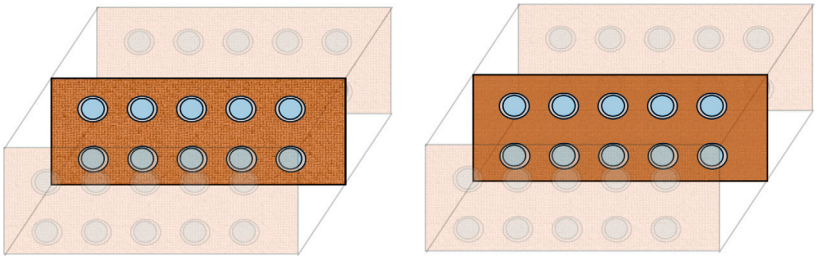

Fig. 2. Simplified schematic of the wool sheets complete pattern experimentally tested in [43].

2.3. Metal wool introduction

In the experiments, the wool sheets of the complete pattern were inserted perpendicularly to the HTF tubes and stacked in the tubes' axial direction as shown in the simplified schematic of Fig. 2 (see [43] for further information).

This configuration, in the numerical geometry considered (shown in Fig. 1(b)) consisted of a 2D plane containing the wool fibers in (quasi) horizontal and vertical directions. In this context, the classical techniques adopted for modeling the composites, i.e. the effective thermophysical properties and the porous media approach, would lead to an incorrect reproduction of the phase transition front shape for this configuration pattern. Even if exploiting different concepts, both mentioned techniques would recreate phase transition fronts starting from the tube boundaries and propagating with concentrical shapes with respect to the tubes. Thus, these techniques would replicate a phase transition behavior similar to that of the bulk PCM, differing only in the faster front propagation rate resulting from the higher local temperature computed in the composite case. However, the addition of the highly conductive metal wool in the 2D axial plane generates several surfaces at which the PCM solidification starts, thus resulting in several phase transition fronts due to the more homogeneous temperature distribution generated by the wool grid. Being the comparison between numerical simulations and experimental measurements solely possible by means of local temperature measurements performed within the PCM, an incorrect modeling of the phase transition front shape would lead to inaccurate results. For these reasons, the introduction of the wool in the numerical model can be performed solely by implementing the wool fibers within the PCM domain considered, thus recreating the wool in the 2D geometry.

The geometrical introduction of the wool fiber in the numerical model inherently poses some challenges. First, the number and the distribution of the wool sheet fibers in the 2D radial plane needed to be estimated. Both factors were derived based on the assumption of an evenly distributed fiber reticulate in the considered 2D plane, as described in Appendix A. This initial assumption led to the estimation of the number of fibers, as the wool mass fraction, wool and PCM densities, and wool mean thickness were known. Subsequently, being the wool sheets different from a regular reticulate, a corrective factor D_{dis} was introduced for taking into account the real distribution and orientation of the fibers, defined as:

$$x_{disord} = x_{ord} + D_{dis} \cdot F \cdot \Delta x_{ord}. \tag{13}$$

Here, the position of the edge of a general fiber in the disordered configuration x_{disord} [cm] is obtained by summing to the evenly distributed position x_{ord} [cm] a corrective term including the D_{dis} term [–], a random function F [–] (which ranges between −1 and 1), and the porous size Δx_{ord} [cm].

In addition, another corrective term was introduced for taking into account the phenomena at the materials interfaces that generally hinder the heat transfer in composite materials. At the wool-PCM interfaces, in fact, non-perfect contacts are present as shown in Fig. 3(b), which depicts an optical microscopy image (at 5x zoom) of the wool-PCM composite. Moreover, the numerical model considers perfectly straight fibers with smooth surfaces, which are properties far from the real fibers, as shown in Fig. 3(a). To take into account these defective behaviors, a penalization term P was introduced to reduce the thermal conductivity of the wool fibers. A reduction in the material thermal conductivity, therefore, was imposed to simulate the real-world properties, a concept that is similar to the mechanical-based thermal interface resistances for nanofiller-based materials [15].

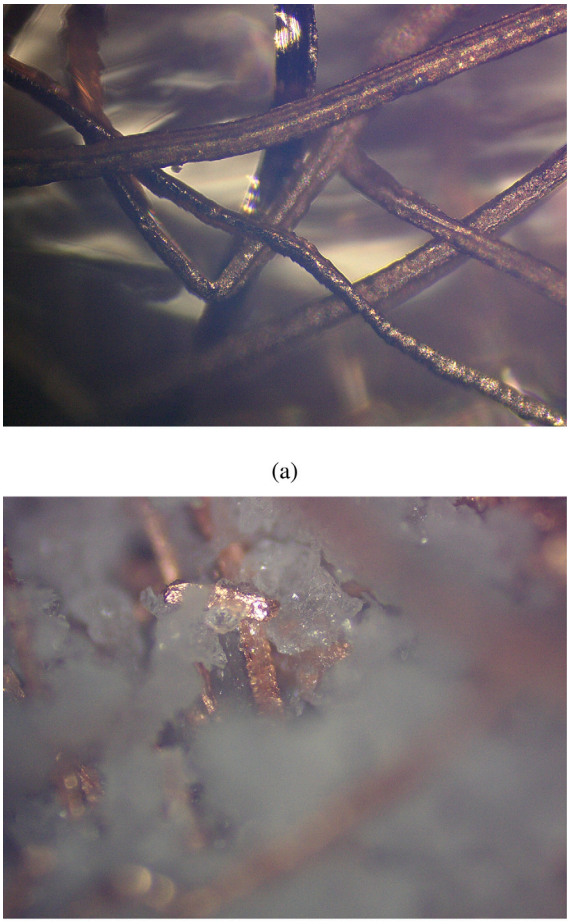

(a)

(b)

Fig. 3. Microscopy images (5x zoom) of the copper wool sheets (a), and copper wool-PCM composite (b) in which the defective wool surfaces and imperfect contact between PCM and wool fibers are visible.

Also for this pattern, the CFD model was coupled with the SOBOL algorithm for obtaining the variation of the input data. The PCM properties were kept the same as the bulk PCM configuration, while:

- The D_{dis} term was considered to vary between 0.1 and 0.9.

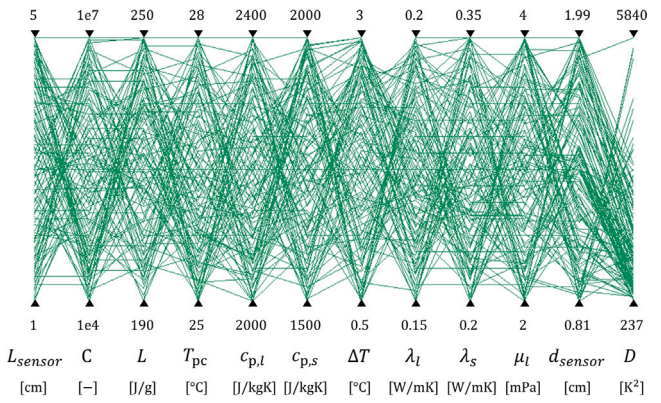

Fig. 4. Parallel coordinates plot for the numerical simulations of the discharging process of the baseline case in which each line represents a numerical simulation. The first eleven columns represent the input parameters, while the last column is the output value, i.e. the difference D shown in Eq. (12).

- The P term varied in a range between 0 and 1.
- The number of fibers was in the range of 10–25 and 20–50 for the thick and fine fibers, respectively.
- The thickness of the fibers was considered ±5% with respect to the nominal values.

3. Results and discussion

3.1. Baseline case - bulk PCM

A total of 139 simulations were conducted by varying the input parameters within the ranges specified in Table 1, following the coupling procedure described in Section 2 between the exploration algorithm and the CFD model. Fig. 4 presents a parallel coordinates plot summarizing the input parameter values used in the simulations and the corresponding target results obtained from Eq. (12). In this plot, each green line represents a numerical simulation, with the parameter values indicated by the intersections of the lines with the corresponding columns.

Thanks to those simulations, a sensitivity analysis over the input parameters was developed with the aim of defining the most influencing ones. An adaptive sparse polynomial chaos expansion technique [53] was adopted, with a resulting R-square of 0.982, and the results are shown by the effect bar chart in Fig. 5. The most impacting factors resulted in the sensor distance and the sensor length, which accounted for more than 75% of the overall impact. Thus, the reconstruction of the sensors' geometrical features in the numerical simulations is of crucial importance when using local temperature measurements, even more important than the accuracy of the materials' thermophysical properties. The results of Fig. 5 also confirm the negligibility of the impact of liquid PCM-related properties during the discharging processes.

Based on the above results, we adopted a purely conductive model in the following numerical simulations, thus saving computational time. This conductive model was validated by comparing it to the complete (conduction+convection) model using the 25 best-matching cases. A negligible difference between the output of the two models was obtained, as shown in Fig. 6 where the percentual differences of the temperatures computed every minute for the 25 curves are plotted against the discharging time. The maximum difference between the two approaches was below 1%, thus validating the sole conductive model.

After this preliminary analysis, a comprehensive study of the PCM thermal behavior during the discharging process was carried out. The input properties range was refined by accurately measuring the length of the sensor in the experimental setup, thus setting it to the constant value of 4 mm (excluding sensor 10, as it had a longer length [43]). The design space of the input parameters was analyzed by performing 100 simulations by means of the SOBOL algorithm, and the comparison of the PCM temperature curves as a function of the discharging process between the 50 best-matching numerical results and the experimental counterparts is plotted in Fig. 7. Here, the dashed line and the corresponding filled region were obtained by computing the average, maximum, and minimum temperature values of the 50 numerical simulations every minute, while the continuous line and the corresponding filled region equals the average and error bars obtained during the experimental tests.

An excellent agreement between experimental measurements and numerical simulations was found, with the exception of two modest discrepancy zones. The first discrepancy zone regards the very first discharging minutes, probably due to (i) the simplifying hypothesis assumed as boundary conditions, and (ii) the reduced size of the TES tank prototype. However, its extent and duration in time is limited (first 20 min). The second discrepancy zone is present at the very last stages of the discharging process. Here, the numerical model predicts a rapid temperature decrease, while the experiments showed only a modest reduction. This discrepancy was attributed to the fact that the RTD sensors experimentally detected the temperature of a mixture composed of PCM and air gaps that resulted from the shrinkage of the PCM due to its solidification. This shrinkage of the PCM is visible in Fig. 8, which shows an experimental picture of the prototype TES tank containing bulk PCM at the end of the discharging process. Those air gaps behaved as insulating regions, thus resulting in the slower temperature decrease detected experimentally by the sensors.

Nonetheless, despite these two modest discrepancy zones, an excellent prediction of the experimental temperature curve was obtained with the proposed numerical approach. This confirmed also that the range of the input parameters chosen was reasonable.

3.2. Wool complete pattern

The discharging processes of the wool-PCM composites (cases 1 and 3 from [43]) were numerically simulated using the same procedure described for the baseline case. The uniform coverage of the design space of the input parameters was obtained by performing 75 simulations. In a preliminary analysis, which is reported in Appendix B, the input parameters range related to the wool, i.e. the D_{dis} term, the P term, and the number of the fibers, were refined in smaller ranges which most likely (in probabilistic terms) would yield numerical results close to the experimental ones. The resulting refined ranges for the input parameters were: D_{dis} between 0.35 and 0.65, P between 0.3 and 0.8, and the number of fibers between 15 and 40 in the case of fine fibers while was kept from 10 to 25 in that of thick fibers. This preliminary analysis aimed at rejecting most of the input values that would have led to outliers in the numerical results.

Then, a comprehensive study was performed with the refined input ranges, and Figs. 9(a) and 9(b) compare the discharging temperature curves from the 50 best-matching numerical cases with the experimental results for copper wool-PCM composites with thick and fine fibers, respectively.

Differently from the baseline case, here a non-negligible discrepancy was present in the phase transition regions, where the numerical model and experimental tests reported different temperature trends. While in the numerical simulations, the theoretical quasi-constant-temperature phase transition (between $T_{pc} + \Delta T$ and $T_{pc} - \Delta T$) is present for a relevant period of time, in the experiments this plateau lasted only some minutes. This experimental behavior may be attributed to the mixture of air gaps, metal wool, and PCM that is present in the proximity of the temperature sensors. Especially the high conductivity of the metal wool fibers may led to the faster temperature decrease detected by the sensors. On the other hand, the discrepancy zone attributed to the PCM shrinkage was present in the last stages of the discharging process also for the PCM-metal wool composite. However, in these

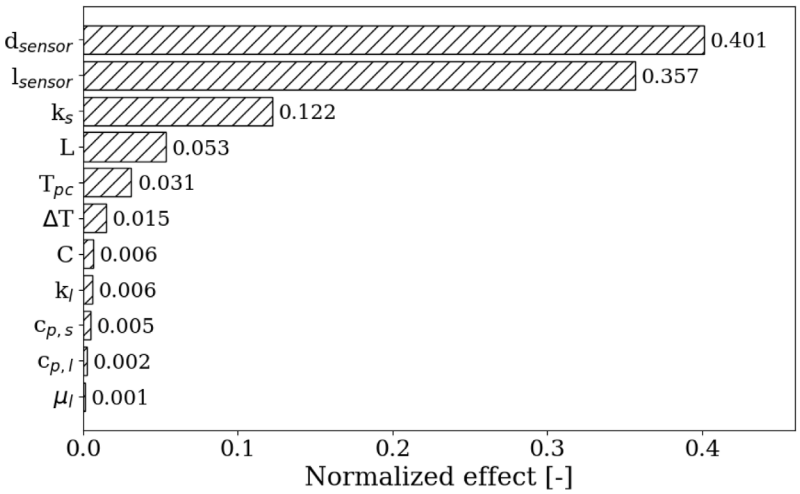

Fig. 5. Results of the sensitivity analysis performed by means of the exploration algorithm and CFD simulations, where the normalized effect represents the relative impact of each input parameter on the simulation output. d_{sensor} and L_{sensor} are the distance from the tube and length of the sensor, respectively; k_s and k_l the solid and liquid PCM thermal conductivities, $c_{p,s}$ and $c_{p,l}$ the solid and liquid PCM specific heat capacities, L the latent heat, T_{pc} the phase transition temperature, ΔT half of the mushy zone, μ_l the dynamic viscosity of the liquid PCM, and C the fitting parameter of the enthalpy porosity method reported in Eq. (8).

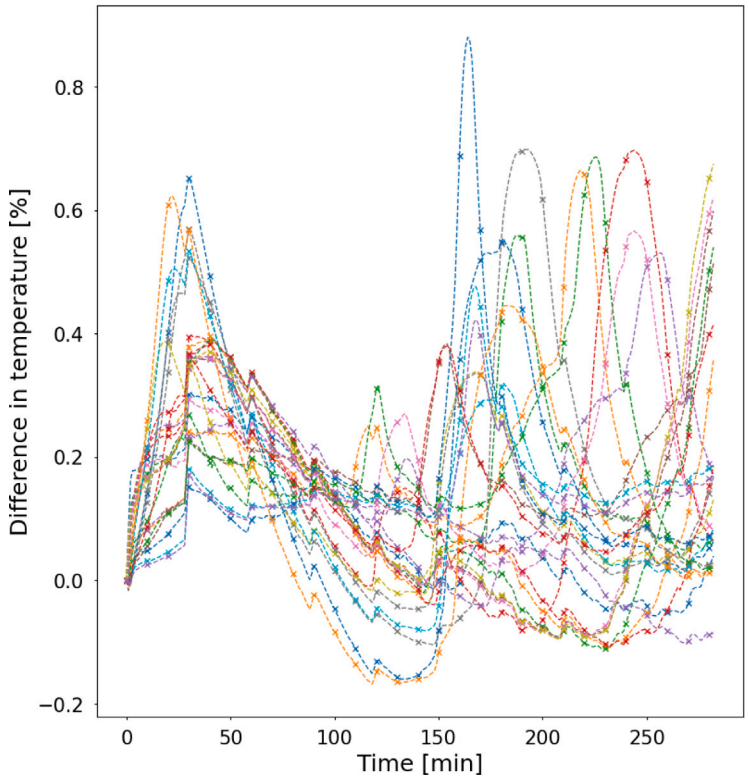

Fig. 6. Difference computed every minute of the 25 best-matching numerical curves obtained by means of the complete and purely conductive model.

composite cases, the experimental temperature decreased more rapidly, and the difference was smaller because the wool fibers partially filled the air gaps that would have otherwise acted as insulators. Despite these relatively small discrepancies due to the difficulty in reproducing such a local phenomenon, overall good agreements were obtained with the proposed numerical model.

After its validation, the model was then used for performing a wool material exploration, by considering aluminum, steel, and iron as possible cheaper alternatives for the copper wool. The comparison was performed by keeping constant the input parameters, thus varying solely the wool materials properties. Thanks to the numerical simulations, a global figure of merit for the comparison was adopted, i.e. the averaged PCM liquid fraction as a function of the discharging time. Fig. 10 reports the comparison between the different materials regarding three figures of merit: the mass fraction of the wool needed to obtain the copper wool-PCM volume fraction experimentally tested (in the upper panel), the time needed to obtain a complete discharging, i.e. to reach a liquid fraction equal to zero in the whole considered domain (in the central panel), and the total cost of the additive material needed to obtain that discharging time (in the lower panel). It is important to stress that the cost here reported is the one of the additive material itself, not the cost of the wool, which also depends on how easily wool fibers can be made out of the bulk material. Fig. 10 can serve as a guideline for selecting wool materials based on the specific

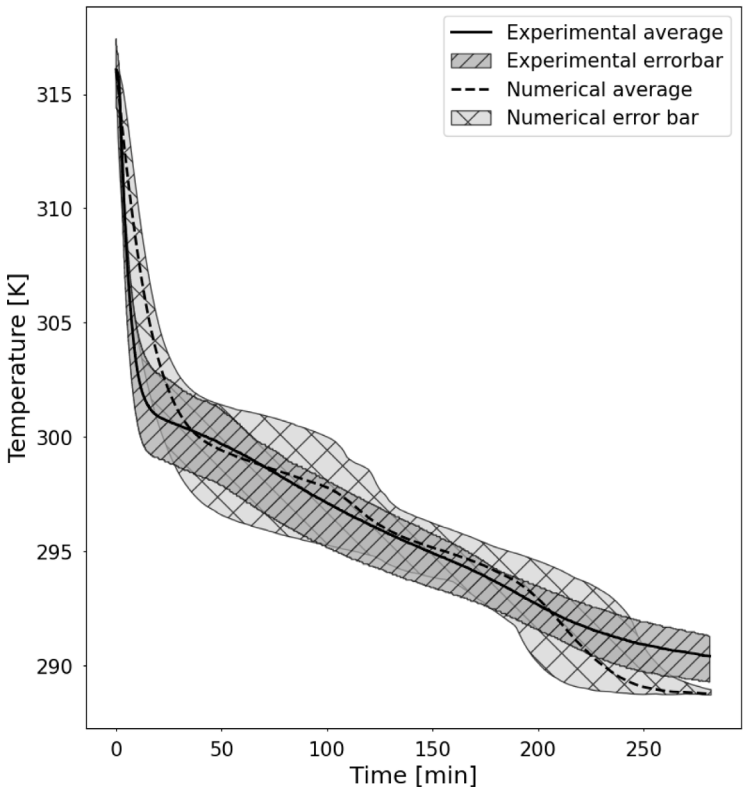

Fig. 7. Comparison between the temperature curves within the PCM during the discharging of the baseline case obtained through the purely conductive numerical model (dashed line) and experimental tests (continuous line). The lines represent the average values, whereas the corresponding filled areas their error bars.

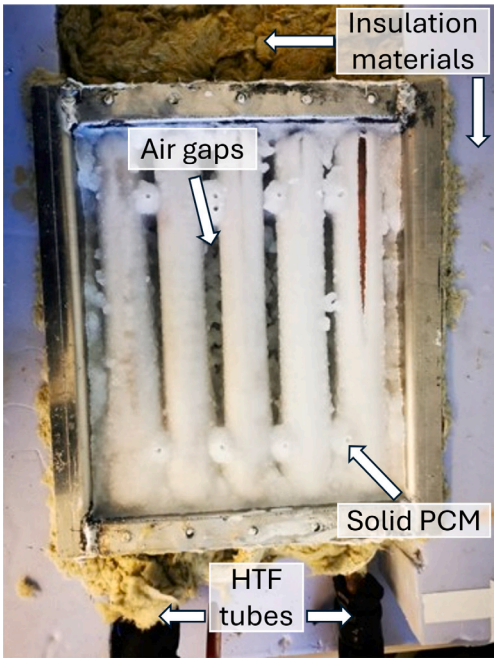

Fig. 8. Experimental image of the TES tank containing bulk PCM after a discharging process, in which the air gaps generated from the shrinkage of the PCM are clearly visible.

requirements of a given application, such as maximum discharging times, weight limitations, or cost constraints. This heat transfer enhancement technique is particularly advantageous for applications that demand relatively fast charging–discharging cycles, including certain power sector applications [34], short- and mid-term TES in the heating and cooling sector [35], and various industrial applications [36]. It is worth mentioning that the discharging time reported here refers to the TES tank prototype experimentally tested in [43]. The related figures of merit — such as charging/discharging times, power, and energy — are thus strictly related to the size of this TES tank. Therefore, a detailed analysis should be performed for each specific storage system, considering factors such as tank size and PCM quantity to accurately assess its performance and compatibility with the application constraints under study. Nonetheless, the analysis reported in Fig. 10 represents an indicative comparison between different wool materials that could be used as heat transfer enhancers in practical TES applications.

3.3. Preliminary cost analysis

In conclusion, a preliminary cost analysis was performed by comparing the proposed case 1 with nanocomposites and metal foams. This analysis used two figures of merit: the thermal conductivity enhancement achieved with the implementation of the copper wool and the cost of the wool material required to achieve this improvement per kilogram of PCM. It is important to note that the cost reported in this analysis refers to the wool fibers, unlike the analysis shown in Fig. 10, which refers to the bulk materials. The thermal conductivity enhancement of the proposed solution was determined by comparing the discharging time curves of the PCM-copper wool composite with thick and fine fibers to those of an equivalent material with an effective thermal conductivity that replicates the discharging behavior of the composite. Fig. 11 shows that an equivalent material with an effective thermal conductivity of 2.5 W/m K resulted in a liquid fraction curve over discharging time similar to the curves obtained with the addition of copper wools. Fig. 12 shows the comparison between the proposed copper wool, nanocomposites, and metal wools in terms of the economic and technical figure of merits mentioned. According to this analysis, the copper wool proposed in this study required a remarkably smaller cost

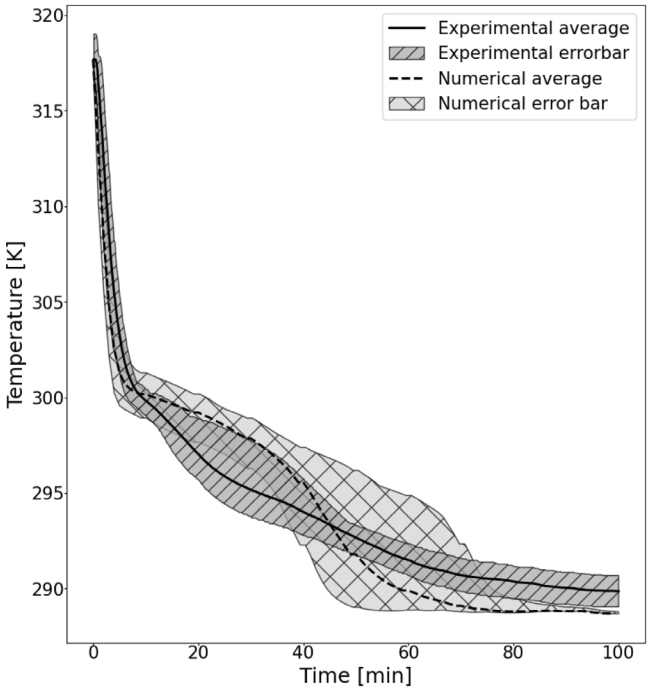

(a)

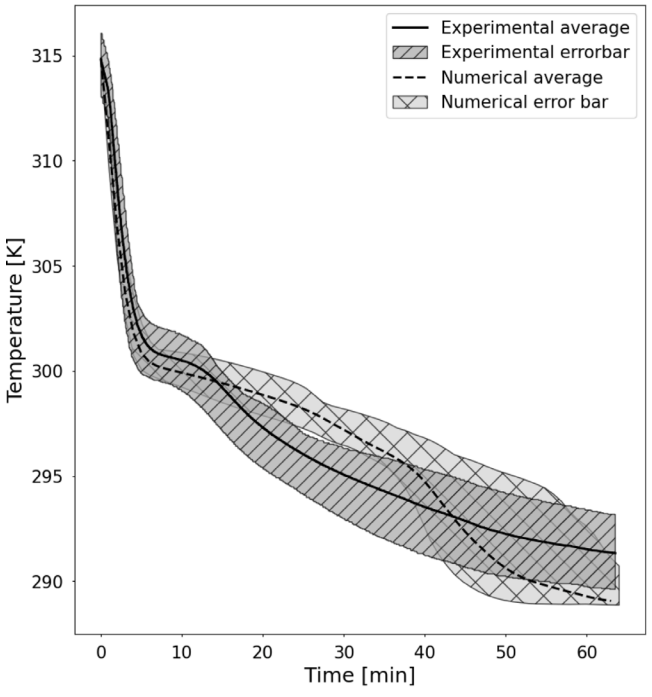

(b)

Fig. 9. Comparison between the temperature curves within the PCM composite during the discharging process of cases 1 (a) and 2 (b) obtained through the purely conductive numerical model (dashed line) and experimental tests (continuous line) [43]. The lines represent the average values, whereas the corresponding filled areas their error bars.

— about 6€ (data obtained April 2024) — with respect to the metal foams (in the order of magnitude of thousands of euros) with a similar thermal conductivity enhancement, while it performed several times better than nanocomposites that possessed similar costs.

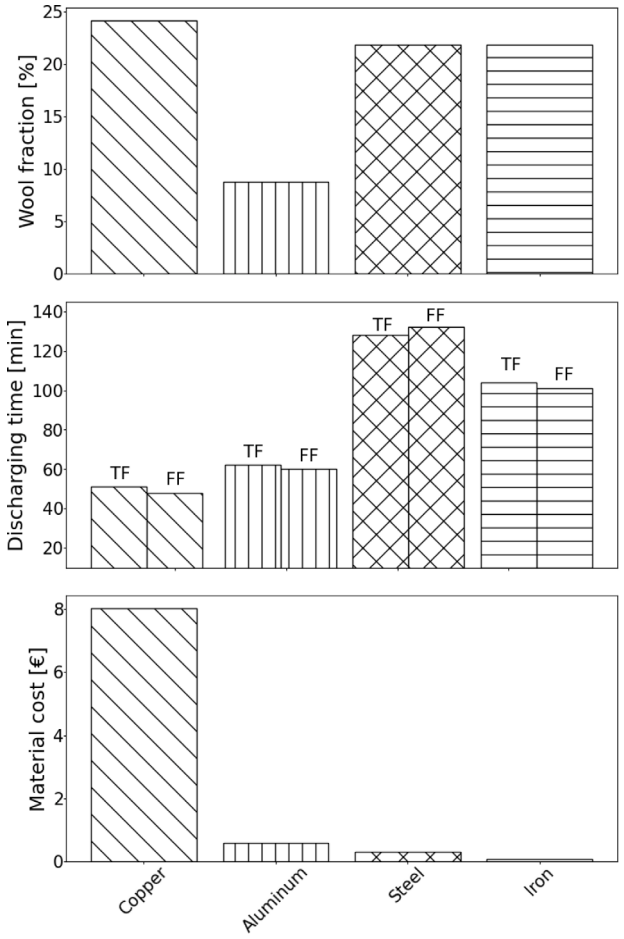

Fig. 10. Overall overview of three figures of merit obtained for different wool materials: the wool mass fraction in the upper panel, the discharging time of the corresponding materials and fiber thicknesses in the central panel, and the costs of the wool materials in the lower panel. TF: thick fibers, FF: fine fibers.

4. Conclusions

In this study, a poorly explored heat transfer enhancement technique obtained by adding metal wool sheets within a PCM matrix was numerically investigated. Numerical simulations of a TES tank prototype containing bulk PCM and PCM-copper wool composite, whose experimental counterparts are reported in [43], have been extensively carried out to obtain a comprehensive assessment of the performance of these novel composite materials.

A coupling between CFD simulations and an explorative algorithm was used to perform a numerical analysis comprehensive of the impact of the accuracy of the input parameters on the output numerical result. At first, a sensitivity analysis of the baseline case (bulk PCM) was performed and revealed the negligible impact of the convective phenomena during the discharging process and the major impact of the geometrical layout of the local temperature measurements. Consequently, a purely conductive numerical model was first validated and then used for the subsequent analysis, thus significantly reducing the computational time without compromising the accuracy. Additional parameters in the numerical model were necessary for the addition of the metal wool, and the simulation of the copper wool-PCM composite yielded good matches between experimental and numerical results, thus validating the reliability of the numerical model. The model was then used to explore different wool materials as cheaper substitutes for the copper that was experimentally tested. The material exploration resulted in an overview of the performance of the metal wool material

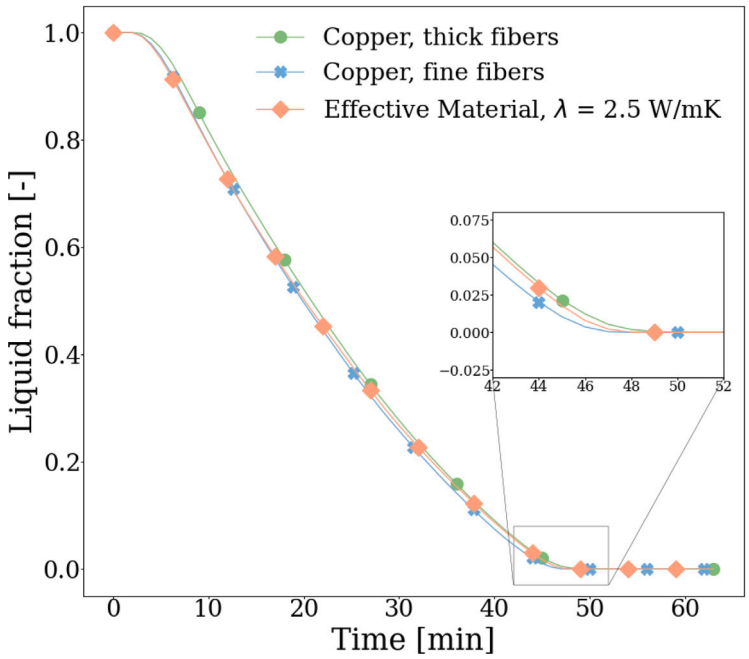

Fig. 11. Comparison between the liquid fractions as a function of the discharging time obtained for the case of fine fiber copper wool, thick fiber copper wool, and an equivalent composite material with an effective thermal conductivity of 2.5 W/m K. The inset plot highlights the time required to achieve complete solidification (when the liquid fraction reaches zero) for all three cases.

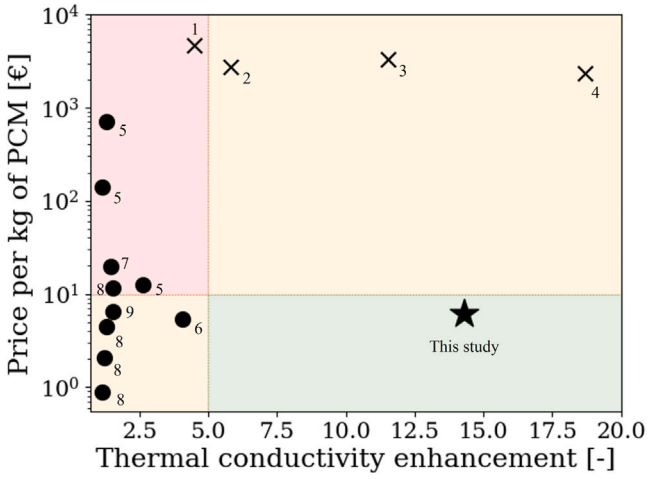

Fig. 12. Comparison between the effective thermal conductivities and costs of heat transfer enhancement materials for 1 kg of PCM considered. The circles denote the nanocomposites, while the 'x' symbol the metal foams. The horizontal line corresponds to the values of 10€, whereas the vertical line indicates a thermal conductivity enhancement of 5, a value that would lead to a thermal conductivity of ~ 1 W/m K for most of the organic PCMs. 1-[56], 2-[57],3-[58],4-[56],5-[59],6-[60],7-[61],8-[62],9-[63].

as a function of the different constraints that may exist in the different case studies, such as the required discharging time, weight, and cost. Additionally, the proposed copper wool-PCM composite was compared to an equivalent PCM with an effective thermal conductivity that replicates the wool-PCM thermal performance, based on the liquid fraction trend over time during the discharging process. As a result, a material with an effective thermal conductivity of 2.5 W/m K was found to match the thermal behavior of the composite in this study, representing a remarkable 14.7-fold increase compared to the bulk PCM value. Finally, the composite with thick fibers of copper wool was compared with the nanocomposites and metal foams techniques from a techno-economic perspective, proving to be a promising solution for enhancing the heat transfer within PCMs in TES applications. In fact, the solution proposed here was the sole one to achieve a thermal conductivity value that may met industrial requirements while ensuring a reduced cost.

In conclusion, this study assesses the possibility of using metal wool as a relatively cheap and effective heat transfer technique, particularly suitable for retrofitting already-built TES tanks. The experimental tests reported in [41–43] and numerical simulations described in this study provide a fundamental groundwork for future optimization and applicative studies, as several areas of improvement are present due to the novel nature of the technique. First, material scale studies could provide insights about the geometrical features of the wool, and their impact on the TES tank thermal performance, in terms of power and energy densities. Moreover, such a material scale study would also lead to a more accurate multi-scale numerical model that may not rely on fitting parameters. Finally, a comprehensive techno-economical analysis, along with experimental tests in pilot plants, could be a further step towards the application of this technique in real-world applications.

Declaration of competing interest

The authors declare that they have no known competing financial interests or personal relationships that could have appeared to influence the work reported in this paper.

Acknowledgments

A.R. and E.C. acknowledge funding under the National Recovery and Resilience Plan (NRRP), Mission 4 Component 2 Investment 1.3—Call for tender No. 1561 of 11.10.2022 of Ministero dell'Università e della Ricerca (MUR); funded by the European Union—NextGenerationEU. This work was partially funded by the Ministerio de Ciencia e Innovacion' - Agencia Estatal de Investigacion' (AEI) (PID2021-123511OB-C31-MCIN/AEI/10.13039/501100011033/ FEDER, UE and RED2022-134219-T). This work is partially supported by ICREA under the ICREA Academia programme. The authors would

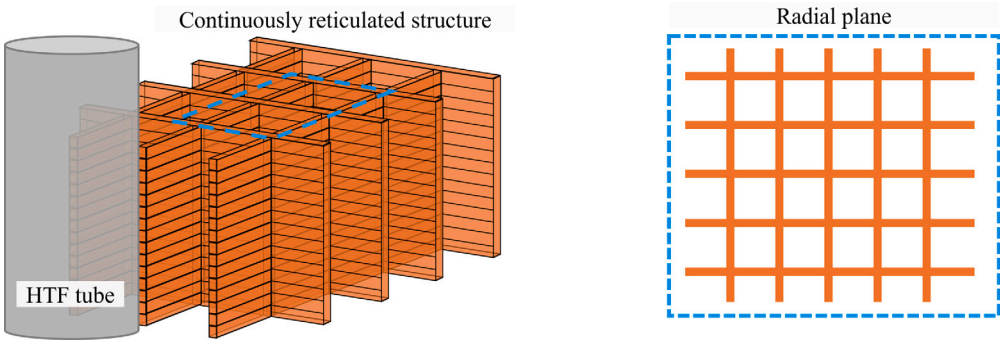

Fig. 13. Schematics of the uniformly distributed continuously reticulated structure (left) and its corresponding radial plane (right).

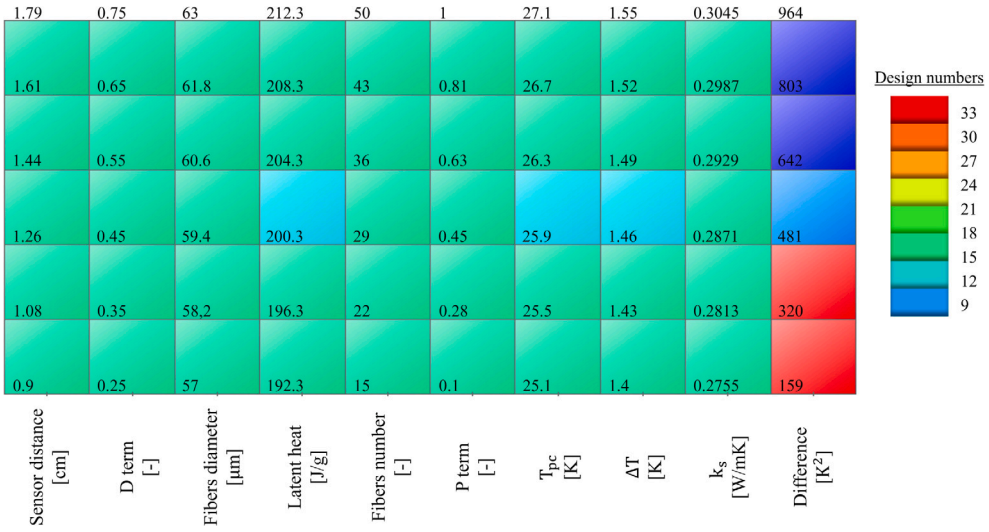

Fig. 14. Frequency analysis of the input parameters (and the output value) from the 75 CFD simulations conducted using the SOBOL algorithm. The color of each box represents how often the specific subrange was used as an input parameter in the numerical simulations.

like to thank the Department de Recerca i Universitats of the Catalan Government for the quality accreditation given to their research group (2021 SGR 01615). GREiA is certified agent TECNIO in the category of technology developers from the Government of Catalonia. This paper is part of the RYC2023-044196-I, funded by MCIU/AEI/10.13039/501100011033 and FSE+. This project has received funding from the European Union's Horizon 2020 research and innovation programme under grant agreement No 101036910

Appendix A

In the composite configurations, wool sheets are placed perpendicular to the tubes until the TES tank is filled, as schematically shown in Fig. 2 and described in [43]. If the fibers were perfectly straight, evenly distributed in the radial plane of the tubes, and had a square cross-section, this geometry could be approximated as a continuously reticulated structure uniformly distributed in space, as illustrated in Fig. 13 left. This initial approximation is based on the fact that the fibers in different wool sheets remain in contact along the tubes' axial direction, as they were placed sequentially upon filling of the TES tank (see Ref. [43] for further details). Given this simplified homogeneous distribution of fibers, the wool volume fraction in the subsystem considered for numerical simulations (see Fig. 1(b)) is assumed to be equal to that of the entire TES tank. Furthermore, the fiber volume fraction in 3D corresponds to the area fraction occupied by fibers in any 2D radial plane (schematized in Fig. 13 right), since the simplified reticulated structure repeats along the tubes' axial direction. The estimated number of fibers in the 2D subsystem can thus be derived from the porosity and adjusted using a corrective factor that accounts for the fibers' circular cross-sectional area. This factor, calculated as the ratio of a circle's area to that of its circumscribed square, led to an estimated fiber count of 31 for fine wool and 14 for thick wool in the considered subsystem.

Appendix B

Fig. 14 is an overview of all the numerical simulations performed for the metal wool-PCM composite (similar to the parallel coordinate plot of Fig. 4): here, each variable range is divided into five subranges, and the color of each subrange indicates the numerosity with which the corresponding parameter appeared in the numerical simulations, based on the SOBOL algorithm. Moreover, also the output parameter D of Eq. (12) is plotted in the last column. Therefore, Fig. 14 confirms the uniform sampling of the input parameters design space achieved through the SOBOL algorithm, being all the subranges of the input parameters of similar colors.

This analysis was ultimately used to identify those input variable ranges likely to lead to numerical results significantly deviating from the experimental curve from a probabilistic perspective. In Fig. 15, the input variable subdomains most frequently used (light blue) in simulations that resulted in significant deviations from the experimental measurements are highlighted by the yellow rectangle. Therefore, these light blue subranges were considered those that can likely be excluded from the analysis due to their tendency to reproduce the thermal behavior of the PCM composite inaccurately. As a result, the remaining subranges (highlighted by the brown rectangles) were

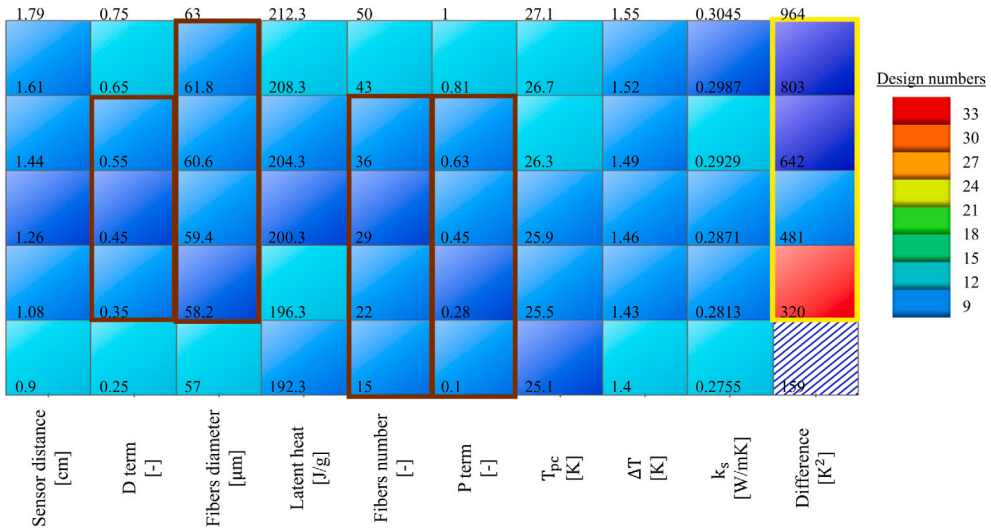

Fig. 15. Frequency analysis of the input parameters (and the output value) corresponding to those simulations that resulted in significant deviations from the experimental measurements (yellow rectangle). On the other hand, the subranges of the fibers input parameter that probabilistically yield more accurate numerical results are those highlighted by brown rectangles.

those that probabilistically yield accurate numerical results, and were adopted in the following analysis.

Data availability

Data will be made available on request.

References

[1] European commission, Report from the Commission To the European Parliament, the Council, the European Economic and Social Committee and the Committee of the Regions, State of the Energy Union, 2022.

[2] H. Mehling, M. Brütting, T. Haussmann, Pcm products and their fields of application - an overview of the state in 2020/2021, J. Energy Storage 51 (2022).

[3] A. Stamatiou, S. Maranda, L.J. Fischer, J. Worlitschek, Solid–Liquid Phase Change Materials for Energy Storage, CRC Press, 2022.

[4] D. Groulx, The Rate Problem in Solid–Liquid Phase Change Heat Transfer: Efforts and Questions Toward Heat Exchanger Design Rules, International Heat Transfer Conference 2018-August, 2018.

[5] L.F. Cabeza, Advances in Thermal Energy Storage Systems (Second Edition), second edition ed., in: Woodhead Publishing Series in Energy, Woodhead Publishing, 2021.

[6] M. Calati, K. Hooman, S. Mancin, Thermal storage based on phase change materials (pcms) for refrigerated transport and distribution applications along the cold chain: A review, Int. J. Thermofluids 16 (2022).

[7] M. Neri, E. Chiavazzo, L. Mongibello, Numerical simulation and validation of commercial hot water tanks integrated with phase change material-based storage units, J. Energy Storage 32 (2020) 101938.

[8] M. Morciano, M. Alberghini, M. Fasano, M. Almiento, F. Calignano, D. Manfredi, P. Asinari, E. Chiavazzo, 3D printed lattice metal structures for enhanced heat transfer in latent heat storage systems, J. Energy Storage 65 (2023) 107350.

[9] R. Saltarelli, L.M. Alves, M. Fasano, R.M. Afonso, Joining by forming technology for thermal applications: A case study of finned tube heat exchanger, Case Stud. Therm. Eng. 59 (2024) 104551.

[10] L. Fan, J.M. Khodadadi, Thermal conductivity enhancement of phase change materials for thermal energy storage: A review, Renew. Sustain. Energy Rev. 15 (2011).

[11] S. Wu, T. Yan, Z. Kuai, W. Pan, Thermal conductivity enhancement on phase change materials for thermal energy storage: A review, Energy Storage Mater. 25 (2020).

[12] A.M. Abdulateef, S. Mat, J. Abdulateef, K. Sopian, A.A. Al-Abidi, Geometric and design parameters of fins employed for enhancing thermal energy storage systems: a review, Renew. Sustain. Energy Rev. 82 (2018) 1620–1635.

[13] W. Ye, D. Jamshideasli, J.M. Khodadadi, Improved performance of latent heat energy storage systems in response to utilization of high thermal conductivity fins, Energies 16 (2023).

[14] Y.-C. Weng, H.-P. Cho, C.-C. Chang, S.-L. Chen, Heat pipe with pcm for electronic cooling, Appl. Energy 88 (2011) 1825–1833.

[15] A. Ribezzo, G. Falciani, L. Bergamasco, M. Fasano, E. Chiavazzo, An overview on the use of additives and preparation procedure in phase change materials for thermal energy storage with a focus on long term applications, J. Energy Storage 53 (2022).

[16] A. Yadav, A. Verma, A. Kumar, H. Dashmana, A. Kumar, P. Bhatnagar, V. Jain, Recent advances on enhanced thermal conduction in phase change materials using carbon nanomaterials, J. Energy Storage 43 (2021) 103173.

[17] A. Al-Ahmed, M.A.J. Mazumder, B. Salhi, A. Sari, M. Afzaal, F.A. Al-Sulaiman, Effects of carbon-based fillers on thermal properties of fatty acids and their eutectics as phase change materials used for thermal energy storage: A review, J. Energy Storage 35 (2021) 102329.

[18] K.Y. Leong, M.R. Abdul Rahman, B.A. Gurunathan, Nano-enhanced phase change materials: A review of thermo-physical properties, applications and challenges, J. Energy Storage 21 (2019) 18–31.

[19] N.S. Dhaidan, S.A. Kokz, F.L. Rashid, A.K. Hussein, O. Younis, F.N. Al-Mousawi, Review of solidification of phase change materials dispersed with nanoparticles in different containers, J. Energy Storage 51 (2022) 104271.

[20] R.P. Singh, H. Xu, D. Rakshit, A. Romagnoli, Charging performance evaluation of finned conical thermal storage system encapsulated with nano-enhanced phase change material, Appl. Therm. Eng. 151 (2019) 176–190.

[21] E.J. D'Oliveira, S.C.C. Pereira, D. Groulx, U. Azimov, Thermophysical properties of nano-enhanced phase change materials for domestic heating applications, J. Energy Storage 46 (2022) 103794.

[22] R. Kumar, A. Mitra, T. Srinivas, Role of nano-additives in the thermal management of lithium-ion batteries: A review, J. Energy Storage 48 (2022) 104059.

[23] B.M.S. Punniakodi, R. Senthil, Recent developments in nano-enhanced phase change materials for solar thermal storage, Sol. Energy Mater. Sol. Cells 238 (2022) 111629.

[24] B.N. Persson, Thermal interface resistance: Cross-over from nanoscale to macroscale, J. Phys. Condens. Matter 26 (2014).

[25] M.M. Sadeghi, I. Jo, L. Shi, Phonon-interface scattering in multilayer grapheme on an amorphous support, Proc. Natl. Acad. Sci. USA 110 (2013).

[26] M. Jurčević, S. Nižetić, M. Arıcı, A.T. Hoang, E. Giama, A. Papadopoulos, Thermal constant analysis of phase change nanocomposites and discussion on selection strategies with respect to economic constraints, Sustain. Energy Technol. Assess. 43 (2021) 100957.

[27] P. Patel, P.P. Bhingole, D. Makwana, Manufacturing, characterization and applications of lightweight metallic foams for structural applications: Review, Mater. Today: Proc. 5 (2018).

[28] T. ur Rehman, H.M. Ali, M.M. Janjua, U. Sajjad, W.M. Yan, A critical review on heat transfer augmentation of phase change materials embedded with porous materials/foams, Int. J. Heat Mass Transfer 135 (2019).

[29] A. Andreozzi, P. Asinari, A. Barletta, V. Bianco, J.A. Bocanegra, P.V. Brandão, B. Buonomo, R. Cappabianca, M. Celli, E. Chiavazzo, et al., Heat transfer and thermal energy storage enhancement by foams and nanoparticles, Energies 16 (2023) 7421.

[30] M. Aramesh, B. Shabani, Metal foam-phase change material composites for thermal energy storage: A review of performance parameters, Renew. Sustain. Energy Rev. 155 (2022).

[31] STAX, Stax website, 2024, https://www.stax.de/en/products/. (Accessed 24 April 2024).
[32] A. Reyes, D. Negrete, A. Mahn, F. Sepúlveda, Design and evaluation of a heat exchanger that uses paraffin wax and recycled materials as solar energy accumulator, Energy Convers. Manage. 88 (2014) 391–398.
[33] H. Mehling, L.F. Cabeza, Heat and Cold Storage with PCM, Springer, 2008.
[34] S. Kuravi, J. Trahan, D.Y. Goswami, M.M. Rahman, E.K. Stefanakos, Thermal energy storage technologies and systems for concentrating solar power plants, Prog. Energy Combust. Sci. 39 (2013) 285–319.
[35] E. Guelpa, V. Verda, Thermal energy storage in district heating and cooling systems: A review, Appl. Energy 252 (2019) 113474.
[36] L. Miró, J. Gasia, L.F. Cabeza, Thermal energy storage (tes) for industrial waste heat (iwh) recovery: A review, Appl. Energy 179 (2016) 284–301.
[37] C. Prieto, A. Lopez-Roman, N. Martínez, J.M. Morera, L.F. Cabeza, Improvement of phase change materials (pcm) used for solar process heat applications, Mol. 26 (2021).
[38] J. Gasia, J.M. Maldonado, F. Galati, M.D. Simone, L.F. Cabeza, Experimental evaluation of the use of fins and metal wool as heat transfer enhancement techniques in a latent heat thermal energy storage system, Energy Convers. Manage. 184 (2019) 530–538.
[39] C. Prieto, C. Rubio, L.F. Cabeza, New phase change material storage concept including metal wool as heat transfer enhancement method for solar heat use in industry, J. Energy Storage 33 (2021).
[40] O. Khliyeva, V. Zhelezny, A. Paskal, Y. Hlek, D. Ivchenko, The effect of metal wool on the charging and discharging rate of the phase transition thermal storage material, Eastern- Eur. J. Enterp. Technol. 4 (2021) 112.
[41] A. Ribezzo, M. Morciano, G. Zsembinszki, S. Risco Amigó, S. Mani Kala, E. Borri, L. Bergamasco, M. Fasano, E. Chiavazzo, C. Prieto, L.F. Cabeza, Enhancement of heat transfer through the incorporation of copper metal wool in latent heat thermal energy storage systems, Renew. Energy 231 (2024) 120888.
[42] A. Ribezzo, M. Morciano, G. Zsembinszki, S.R. Amigo, S.M. Kala, E. Borri, L. Bergamasco, M. Fasano, E. Chiavazzo, L. Cabeza, Assessing the impact of copper wools on a phase change material-based tes tank prototype, J. Phys.: Conf. Ser. 2766 (2024) 12234.
[43] S.M. Kala, A. Ribezzo, G. Zsembinszki, E. Borri, C. Prieto, L.F. Cabeza, Development of copper metal wool incorporated in a latent thermal energy storage tank for improved charging and discharging, Appl. Therm. Eng. 2025 (1255) 049.
[44] M. Mahfuz, M. Anisur, M. Kibria, R. Saidur, I. Metselaar, Performance investigation of thermal energy storage system with phase change material (pcm) for solar water heating application, Int. Commun. Heat Mass Transfer 57 (2014) 132–139.
[45] D. Dzhonova-Atanasova, A. Georgiev, S. Nakov, S. Panyovska, T. Petrova, S. Maiti, Compact thermal storage with phase change material for low-temperature waste heat recovery—advances and perspectives, Energies 15 (2022) 8269.
[46] S. COMSOL AB, COMSOL User's Guide, Stockholm, 2024.
[47] A. Martínez, M. Carmona, C. Cortés, I. Arauzo, Experimentally based testing of the enthalpy-porosity method for the numerical simulation of phase change of paraffin-type pcms, J. Energy Storage 69 (2023) 107876.
[48] B. Niezgoda-Zelasko, The enthalpy-porosity method applied to the modelling of the ice slurry melting process during tube flow, Procedia Eng. 157 (2016) 114–121.
[49] M. Goderis, A. Buruzs, F. Giordano, T. Barz, W. Beyne, M. De Paepe, Numerical modelling of thermal hysteresis in melting and solidification of phase change materials, J. Phys.: Conf. Ser. 2766 (2024) 012227.
[50] M. Faden, S. Höhlein, J. Wanner, A. König-Haagen, D. Brüggemann, Review of thermophysical property data of octadecane for phase-change studies, Mater. 12 (2019) 2974.
[51] A. Gil, C. Barreneche, P. Moreno, C. Solé, A. Inés Fernández, L.F. Cabeza, Thermal behaviour of d-mannitol when used as pcm: Comparison of results obtained by dsc and in a thermal energy storage unit at pilot plant scale, Appl. Energy 111 (2013) 1107–1113.
[52] A. Svobodova-Sedlackova, A. Calderón, X. Sanuy-Morell, M. Neira-Viñas, M. Majó, C. Barreneche, P. Gamallo, A. Inés Fernandez, Using statistical analysis to create a new database of nanofluids' specific heat capacity, J. Mol. Liq. 369 (2023) 120847.
[53] ESTECO, ModeFrontier user's manual, 2024.
[54] A. Abdi, M. Ignatowicz, S.N. Gunasekara, J.N. Chiu, V. Martin, Experimental investigation of thermo-physical properties of n-octadecane and n-eicosane, Int. J. Heat Mass Transfer 161 (2020) 120285.
[55] Y. Kozak, G. Ziskind, Novel enthalpy method for modeling of pcm melting accompanied by sinking of the solid phase, Int. J. Heat Mass Transfer 112 (2017) 568–586.
[56] M.M. Elidi, M. Karkri, M. Kraiem, Preparation and effective thermal conductivity of a paraffin/ metal foam composite, J. Energy Storage 33 (2021) 102077.
[57] A. Hussain, C. Tso, C.Y. Chao, Experimental investigation of a passive thermal management system for high-powered lithium ion batteries using nickel foam-paraffin composite, Energy 115 (2016) 209–218.
[58] T. Li, D. Wu, F. He, R. Wang, Experimental investigation on copper foam/hydrated salt composite phase change material for thermal energy storage, Int. J. Heat Mass Transfer 115 (2017) 148–157.
[59] L.-W. Fan, X. Fang, X. Wang, Y. Zeng, Y.-Q. Xiao, Z.-T. Yu, X. Xu, Y.-C. Hu, K.-F. Cen, Effects of various carbon nanofillers on the thermal conductivity and energy storage properties of paraffin-based nanocomposite phase change materials, Appl. Energy 110 (2013) 163–172.
[60] B. Praveen, S. Suresh, Experimental study on heat transfer performance of neopentyl glycol/cuo composite solid–solid pcm in tes based heat sink, Eng. Sci. Technol. an Int. J. 21 (2018) 1086–1094.
[61] V. Kumaresan, R. Velraj, S.K. Das, The effect of carbon nanotubes in enhancing the thermal transport properties of pcm during solidification, Heat Mass Transf. 48 (2012) 1345–1355.
[62] A. Ribezzo, L. Bergamasco, M. Morciano, M. Fasano, L. Mongibello, E. Chiavazzo, Experimental analysis of carbon-based phase change materials composites for a fast numerical design of cold energy storage systems, Appl. Therm. Eng. 231 (2023) 120907.
[63] K.P. Venkitaraj, S. Suresh, B. Praveenand, A. Venugopal, S.C. Nair, Pentaerythritol with alumina nano additives for thermal energy storage applications, J. Energy Storage 13 (2017) 359–377.